

## Intrinsic instability to martensite phases in ferromagnetic shape memory alloy $\text{Ni}_2\text{MnGa}$ : Quasiparticle self-consistent $GW$ investigation

Masao Obata <sup>1</sup>, Takao Kotani <sup>2,3</sup> and Tatsuki Oda <sup>1,3</sup>

<sup>1</sup>Graduate School of Natural Science and Technology, Kanazawa University, Kanazawa 920-1192, Japan

<sup>2</sup>Advanced Mechanical and Electronic System Research Center, Department of Engineering, Tottori University, Tottori 680-8552, Japan

<sup>3</sup>Center for Spintronics Research Network, Osaka University, Toyonaka 560-8531, Japan

 (Received 23 March 2022; revised 24 November 2022; accepted 31 January 2023; published 21 February 2023)

We investigated the electronic structure of a ferromagnetic shape memory alloy  $\text{Ni}_2\text{MnGa}$  utilizing an advanced approach, quasiparticle self-consistent  $GW$ , which takes account of electron localization effects without empirical parameters. The Ni  $e_g$  orbitals in the cubic phase, which lead to martensite phase transition, were found to locate on the Fermi level, implying a clear definitive origin of band Jahn-Teller (JT) effect in comparison with the results obtained by the density functional approach of generalized gradient approximation. From the analysis of generalized susceptibility in the cubic phase, the instabilities responsible for the modulated structures of 10M, 14M, and 6M were found to be an intrinsic property in the electronic states. These states may stabilize the modulated one, accompanied by tetragonal local JT distortions. Their property of Fermi surface nesting sensitively depends on a subtle change in the magnetic moment, corresponding to the experimental fact that the modulated structure appears depending on temperature and the composition of the magnetic element. The secondary nesting vector along [110] direction was discussed in relation to a modulation alignment of the nanotwin boundary.

DOI: [10.1103/PhysRevMaterials.7.024413](https://doi.org/10.1103/PhysRevMaterials.7.024413)

### I. INTRODUCTION

Ferromagnetic shape memory alloys possess magnetic and shape memory properties and exhibit significant shape distortions due to external magnetic fields and temperature changes. The shape memory property requires twin boundaries to relax the interfacial strain caused by the martensite transition. In addition, both of their high mobility due to an external magnetic field and large magnetic anisotropy in the twin boundaries are the keys to yielding a sizable magnetic field-induced strain (MFIS). In particular, the Heusler alloy, Ni-Mn-Ga [1–5], possesses giant MFIS of more than 10% and magnetocaloric properties [6,7], having a high potential for many technological applications, such as magnetic actuators, sensors [8], and refrigerants [9]. The high-temperature phase, austenite in the  $L2_1$  structure, undergoes martensitic transformation upon cooling. Interestingly, several modulated martensitic structures, namely 6M (pre-martensitic), 10M [10], and 14M [11], have been observed experimentally [12]. In the latter two structures, the nanometer scale twinned boundary (nanotwin boundary) is a key to the modulation [13]. For the stoichiometric composition of  $\text{Ni}_2\text{MnGa}$ , the 10M structure is the most stable at low temperatures, while for the nonstoichiometric compositions, the 14M and nonmodulated (NM) martensitic structures also appear, depending on their composition. They tend to appear at room temperature in the order of 10M, 14M, and NM as the number of valence electrons increases [14]. In these modulated structures, the low migration energy barrier of the nanotwin boundaries results in the MFIS. The 6M structure is observed only at a few

Kelvin above the temperature of martensite phase transition, associated with anomalous softening of the transverse phonon modes ( $\text{TA}_2$ ) along the wave vectors of [110] direction [15]. Since Fermi surface nesting is considered a driving force to martensitic transformation, the Fermi surface geometry and generalized susceptibility have been investigated based on the first-principles approach within local density approximation (LDA) and generalized gradient approximation (GGA) [16–23]. The nesting vector appears along the [110] direction, denoted as  $[\xi, \xi, 0]2\pi/a$ , where  $a$  is the lattice constant of the austenite cubic phase. LDA/GGA calculations yielded a nesting vector of  $\xi = 0.4$ , which was considered an overestimation for  $\xi = 1/3$ , specifying the 6M structure. Such a nested electronic structure supports the formation of a charge density wave (CDW). The incommensurate nesting vector for the pre-martensite phase was observed together with the pseudogap at the Fermi level [24].

It is evident from the previous studies above that the nesting vectors for 10M and 14M have not yet emerged in theoretical works, forcing researchers to interpret the 10M and 14M structures as a competition between the Jahn-Teller (JT) effect and  $\text{TA}_2$  mode softening [15]. The long history of research work on  $\text{Ni}_2\text{MnGa}$  has not indicated that the origin of their structural stabilization of 10M and 14M is well understood.

To understand the mechanism stabilizing the martensite phases, we need a reliable description of the electronic structure for  $\text{Ni}_2\text{MnGa}$ . On top of the electronic structure, we can consider entropic effects [6] by the method proposed in Ref. [25]. Furthermore, we can use the coherent-potential

approximation (CPA) or supercell calculation to investigate properties of elastic constant and magnetic moment in the nonstoichiometric composition [26]. The substitution effects at the Ga site ( $\text{Ni}_2\text{Mn}_{1+x}\text{Ga}_{1-x}$ ) were reported on their magnetic and magnetoelastic properties [26]. The authors found that an antiferromagnetic coupling between Mn atoms on the Ga sublattice and Mn atoms on the Mn sublattice favors at the composition of  $x \sim 0.25$  over the ferromagnetic coupling. The supercell GGA calculations yielded results that may contradict the experimental facts; for instance, in terms of internal energy, 10M is more unstable than NM [27], and the hypothetical two-period 4O structure is the most stable in several modulated structures [28]. Consequently, the focus has been on the reliability of LDA/GGA, with studies applying the GGA+ $U$  and meta-GGA methods to probe the reliability of GGA [29,30]. The results show that the modulated martensite phase is more energetically stable than the NM phase, supporting the importance of electron correlation effects [31,32]. In addition, GGA +  $U$  reveals that the stability of the austenite and martensite phases is highly dependent on the value of  $U$  [29]. However, the validity of GGA +  $U$  has not been fully discussed, as existing research has been solely based on comparisons with specific experimental values such as crystal structure, bulk modulus, and magnetic moments [33].

The theoretical facts mentioned in the previous paragraph suggest that GGA and GGA +  $U$  methods are limited in describing the electronic structure of  $\text{Ni}_2\text{MnGa}$  for understanding the martensitic mechanism. This is somehow related to the nature of  $\text{Ni}_2\text{MnGa}$  where we treat two kinds of transition metals whose  $3d$  bands are formed around the Fermi energy. Thus, we need to seek a reliable description of electronic structures beyond such theories; not only  $3d$  bandwidths and positions but also the hybridization with  $sp$  bands. These control the band-energy gain for phase transitions.

In this paper, we present results based on a reliable electronic structure calculation via the quasiparticle self-consistent  $GW$  (QSGW) method [34–36]. Among existing state-of-the-art electronic structure calculations, QSGW is a general-purpose first-principles method to improve the drawbacks of GGA and GGA +  $U$ . It determines the optimum independent-particle picture of electrons in a manner of the self-consistent  $GW$  approximation [37]. Since it is established that QSGW works well for the electronic structure investigations of various materials, such as oxides and semiconductors [38,39], it has recently been applied to metals and magnetic materials [40–42]. Furthermore, QSGW has even more advantages over the conventional density functional theory (DFT) approaches; no empirical parameter such as  $U$  and inclusion of a proper electron correlation due to electron localization. In the present study, we investigate electronic structures and magnetic properties of the cubic (austenite) and tetragonal (martensite) phases in metallic  $\text{Ni}_2\text{MnGa}$ . Our results revealed that a nesting vector appears at the modulations of 6M, 10M, and 14M, depending on the condition of the rigid-band approach. Results for GGA and GGA +  $U$  are also presented for comparison with QSGW to discuss its electron correlation effects and differences from the conventional methods.

## II. COMPUTATIONAL DETAILS

This section briefly describes the QSGW method and details of the computation. First-principles  $GW$  calculations [43], which apply Hedin's  $GW$  approximation [37] to first-principles calculations, have achieved a lot of success in analyzing and predicting the electronic structure of semiconductors or insulators. However, the  $G_0W_0$  approach, widely used in first-principles  $GW$  calculation, is just a perturbation calculation for the self-energy of electrons, often called the one-shot  $GW$ . In the one-shot  $GW$  based on the mean-field Hamiltonian ( $H_0$ ) of LDA/GGA, the Green's function ( $G_0$ ) and the screened Coulomb matrix ( $W_0$ ) with a random-phase approximation calculated from  $H_0$ 's eigenfunctions and eigenvalues have been used to evaluate self-energy ( $iG_0W_0$ ). Unfortunately, the one-shot approach suffers from dependence on the starting point, causing an uninvited depletion of its validity since the starting Hamiltonian ( $H_0$ ) becomes inaccurate for correlated electron systems, such as localized  $d$ - or  $f$ -electron systems [44]. The starting point problem with metals is rather clear, as the occupied states in the mean-field Hamiltonian can move up to unoccupied states in the one-shot  $GW$ . Hence, this approach has remained unsatisfactory because its mean-field potential is inconsistent with the resulting electronic structure.

QSGW was proposed as a relatively simplified approach so as to solve these problems by constructing a better mean-field potential based on the  $GW$  self-energy [35,36]. Updating the mean-field Hamiltonian in the QSGW framework allows the application of  $GW$  calculations to systems where LDA/GGA is not an appropriate starting point. As a result, the electronic structure can be substantially improved by such a self-consistent iterative procedure.

From another point of view, QSGW is for determining the optimum independent-particle picture within a quasiparticle-based perturbation theory [39]. Generally speaking, we expect not only the contribution (off-site), correcting band gap, and effective mass for semiconductors [38], but also  $U$ -type contributions (on-site) in QSGW. These contributions correspond to two types of nonlocality (off-site and on-site) of self-energy [42]. Relative to GGA, QSGW tends to make the  $3d$  bands narrower and being pushed down relative to the anion  $p$  bands [45,46], while the width of anion  $p$  bands is usually enlarged [47].

Figure 1 shows the tetragonally distorted  $L2_1$  crystal structure ( $a$  and  $c$  represent the in-plane and out-of-plane lattice constants) and its first Brillouin zone (BZ) of  $\text{Ni}_2\text{MnGa}$ . In the present study, the systems of  $c/a = 1.00, 1.10, 1.20,$  and  $1.25$  were investigated assuming the constant volume of  $98.823 \text{ \AA}^3/\text{f.u.}$ , which was experimentally obtained in the cubic phase ( $c/a = 1.00$ ) [48]. The  $c/a = 1.20$  is close to the experimental values of  $1.207$  [49] and  $1.18 \pm 0.02$  [50]. We employed a body-centered tetragonal primitive cell in the calculation. The tetragonal Bravais lattice (in-plane lattice constant  $a' = a/\sqrt{2}$ ) corresponds to the gray area in Fig. 1(a), and its primitive cell contains two Ni, one Mn, and one Ga atoms.

The QSGW, GGA +  $U$ , and GGA calculations were performed using a mixed basis all-electron first-principles

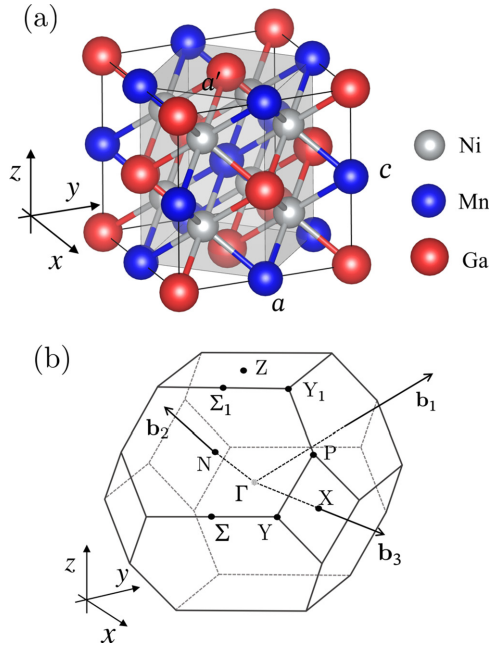


FIG. 1. Crystal structure (a) and first Brillouin zone (b) of  $\text{Ni}_2\text{MnGa}$ .  $\mathbf{b}_1$ ,  $\mathbf{b}_2$ , and  $\mathbf{b}_3$  indicate reciprocal lattice vectors of the body-centered tetragonal cell.

package ecalj [38,51–54]. The  $k$ -point samplings of  $16 \times 16 \times 16$  and  $8 \times 8 \times 8$  were adopted for the GGA and GW parts, respectively. All our GGA calculations employ the Perdew, Burke, and Ernzerhof (PBE) version in the exchange-correlation functionals [55]. For the GGA +  $U$  calculation [56], we adopted an on-site Coulomb correction of  $U = 1.8$  eV on Mn atom, which seems to be suitable for  $\text{Ni}_2\text{MnGa}$  so that the optimized lattice parameters become close to those of experiments [31,32]. This  $U$  means an effective  $U$  in Dudarev’s approach [57], coupled with the projected component onto the  $3d$  orbitals inside their muffin-tin sphere. The muffin-tin sphere radii were chosen to be 1.25 and 1.20 Å for Mn/Ga and Ni atoms, respectively. Self-consistent iterations of the QSGW calculation were performed until the change in quasiparticle energy eigenvalue was less than 0.005 eV for all orbitals and  $k$  points.

The generalized susceptibility  $\chi^\rho(\mathbf{q})$  of each spin state can be written as follows:

$$\chi^\rho(\mathbf{q}) = \frac{1}{N_{\mathbf{k}}} \sum_{n,m,\mathbf{k}} \frac{f_{m\mathbf{k}+\mathbf{q}}^\rho - f_{n\mathbf{k}}^\rho}{\varepsilon_{n\mathbf{k}}^\rho - \varepsilon_{m\mathbf{k}+\mathbf{q}}^\rho}, \quad (1)$$

where  $\mathbf{q} = (q_x, q_y, q_z)$  and  $\mathbf{k} = (k_x, k_y, k_z)$  represent the wave vectors in the first BZ,  $N_{\mathbf{k}}$  is the number of  $k$  points,  $n$  and  $m$  are the band indices,  $\rho$  is the spin index ( $\uparrow, \downarrow$ ),  $\varepsilon_{n\mathbf{k}}^\rho$  are the energy eigenvalues, and the  $f$ ’s are the occupations of the Fermi distribution function. The total generalized susceptibility  $\chi$  is the sum of  $\chi^\uparrow$  and  $\chi^\downarrow$  ( $\chi = \chi^\uparrow + \chi^\downarrow$ ). Note that the peak on the  $\chi(\mathbf{q})$ , corresponding to the Fermi surface nesting, may indicate a possible instability to the modulation given by its wave vector  $\mathbf{q}$ .

For the  $\chi$  calculation, a  $k$ -point sampling of  $192 \times 192 \times 192$  in the cubic BZ was used. For the smearing of the Fermi surface, an electron temperature of 10 K was adopted

in the Fermi distribution function. We considered the pairs with energy differences within 6 eV to fully incorporate the transitions between  $d$  channels. This energy cutoff is large enough to catch the properties of  $\chi$  because, as shown in Eq. (1), the pair of energy eigenvalues with a slight energy difference between the occupied and unoccupied states may mainly contribute to  $\chi$ .

Based on the rigid-band model, we investigated a chemical potential dependence of  $\chi$ . This model is a useful simple approximation for studying the changes in electronic properties with electron/hole doping and magnetic moment changes. In this approach, we suppose quasiparticle eigenvalues to be robust to changes in chemical potential. The number of electrons in the majority (minority) spin state,  $N^\uparrow(N^\downarrow)$ , is calculated as a function of the chemical potential  $\mu^\rho$ :  $N^\rho(\mu^\rho) = \sum_{n\mathbf{k}} f_{n\mathbf{k}}^\rho(\mu^\rho)/N_{\mathbf{k}}$ . The number of electrons  $N$  is  $N^\uparrow + N^\downarrow$  and the magnetic moment  $M$  is  $N^\uparrow - N^\downarrow$ . Using  $\varepsilon_{n\mathbf{k}}^\rho$ , we determined the chemical potential ( $\mu^\uparrow$  and  $\mu^\downarrow$ ) of each spin state for a given set of  $\Delta n$  and  $\Delta m$  ( $N = N_0 + \Delta n$  and  $M = M_0 + \Delta m$ , where  $N_0$  and  $M_0$  are, respectively, the number of electrons and magnetic moment obtained by the self-consistent calculation). These obtained chemical potentials were adopted in Eq. (1). We mainly investigated within the following range:  $-0.5 \mu_{\text{B}}/\text{f.u.} \leq \Delta m \leq 0.16 \mu_{\text{B}}/\text{f.u.}$  and  $\Delta n = 0$ . The case of large negative  $\Delta m$  corresponds to a model for suppressing magnetic moments due to the effects of temperature fluctuations; for example, field-induced saturation magnetization is reduced by around 10% ( $\sim 0.4 \mu_{\text{B}}/\text{f.u.}$ ) at the temperature of martensitic transformation compared to that of low temperatures [58–60]. Conversely, one may consider the positive  $\Delta m$  for a slight increase in Mn composition. Some excessive Mn substitution, in which the additional Mn atom tends to occupy the Ga site, causes antiferromagnetic couplings in nonstoichiometric compositions, as described in Refs. [26,61]. Therefore the net magnetic moment does not increase: a large positive  $\Delta m$  is not realistically expected. At the final stage of the investigation, as reported in Sec. III G, we took the ranges of  $-0.2 e/\text{f.u.} \leq \Delta n \leq 0.6 e/\text{f.u.}$  and  $-0.8 \mu_{\text{B}}/\text{f.u.} \leq \Delta m \leq 0.8 \mu_{\text{B}}/\text{f.u.}$

Overall, the QSGW calculation is much more computationally expensive than the standard GGA calculations and currently does not allow us to access the total internal energy. Therefore, methods that are based on the total energy functional and adaptable in large systems, such as the GGA +  $U$  method, are also essential for applications. In our investigation, it is also vital to confirm the accuracy and validity of GGA +  $U$ .

### III. RESULTS AND DISCUSSION

#### A. Overall features of electronic structure

The results of QSGW show a lot of improved features in the electronic structure. For instance, as shown in Figs. 2 and 3, the Ni  $3d e_g$  component of the minority spin state appears just at the Fermi level for the cubic phase ( $c/a = 1.00$ ). This can be definitive theoretical evidence for the existence of phase instability at low temperatures. Compared with the GGA +  $U$  or GGA results, the eigenvalue levels of the minority spin state shift to higher energies, indicating

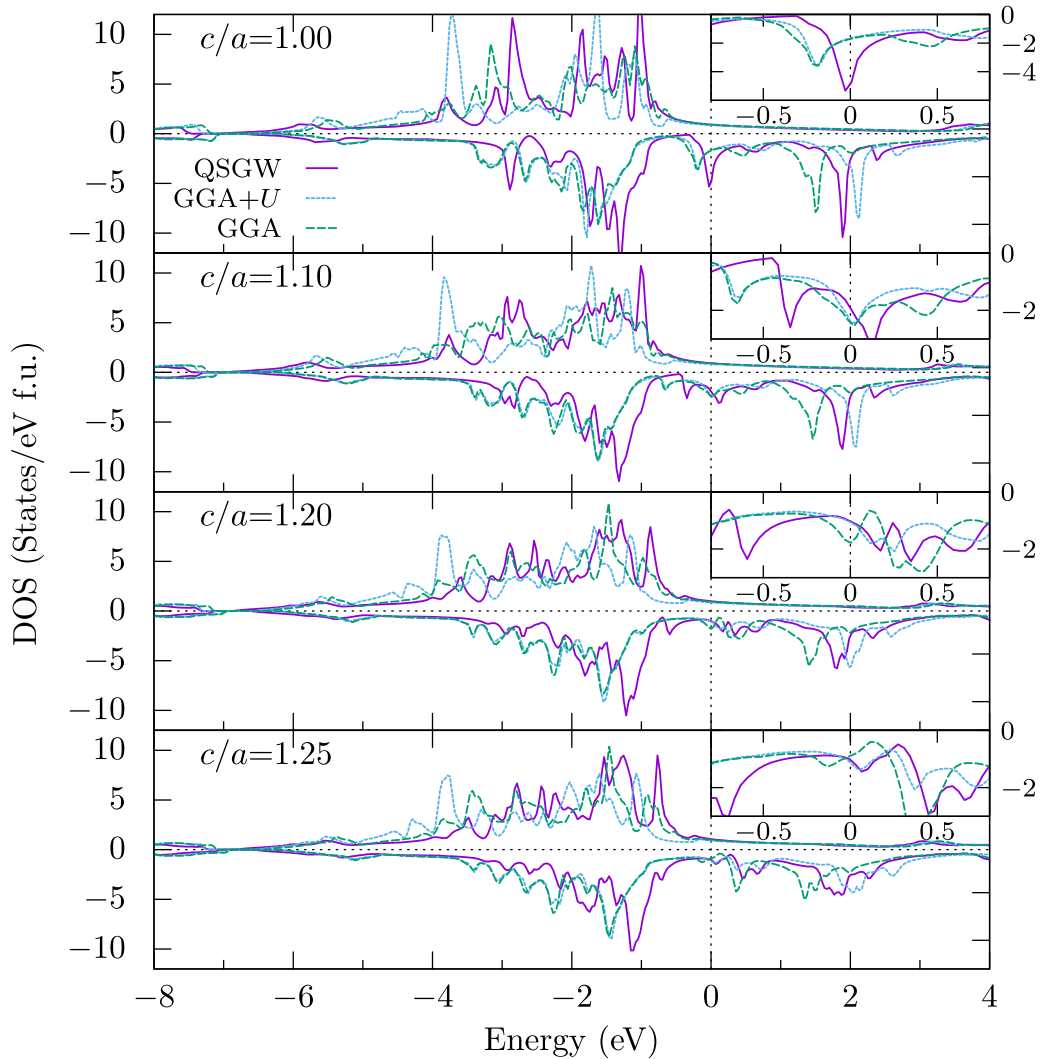


FIG. 2. Total density of states (DOS) calculated by QSGW (solid lines), GGA +  $U$  (dotted lines), and GGA (dashed lines) (the vertical axis of the inset is shown on the right side). The insets show enlarged minority spin components of DOS within a range of  $-0.8$  to  $0.8$  eV from the Fermi level.

an increase in exchange splitting and, thus, an increasing total magnetic moment. This feature implies an increase in magnetic energy in the advanced theoretical approach. The energy level shift, appearing at the Fermi level, in the minority spin state is small but makes a drastic change in the generalized susceptibility. The change is quantitative, but the meaning of its result provides a qualitative conclusion in the martensite phase of 10M or 14M appearing at low temperatures. Such an instability indicated from the investigation of susceptibility is found to be much more sensitive to the magnetic moment, implying a close relationship with the composition of the magnetic element and the external magnetic field. The later sections describe details of the results and discussions.

### B. Density of states

Figure 2 shows the total density of states (DOS) for the majority and minority spin states. This figure notably reveals a large exchange splitting, indicating the presence of a large

total magnetic moment. Focusing on the vicinity of the Fermi level, the DOS of the minority spin state sensitively depends on the structural parameter  $c/a$ . The large DOS at the Fermi level in  $c/a = 1.00$  (cubic phase) separates into occupied and unoccupied peaks as  $c/a$  increases. Such a separation of DOS peaks near the Fermi level is a consequence of the structural transformation from the cubic (austenite) phase to the tetragonal phase. This is typical behavior in the band JT effect [62]. The decrease near the Fermi level in the DOS ( $c/a > 1$ ) through the transformation is consistent with what has been reported experimentally in Ni-Mn-Ga systems [24,63,64]. The results show that, for all values of  $c/a$ , there are visible differences between QSGW and the others (GGA and GGA +  $U$ ).

We particularly focus on two results: The DOS at the Fermi level for  $c/a = 1.00$ . At this point, although QSGW shows a remarkable peak just on the Fermi level, a corresponding GGA (or GGA +  $U$ ) peak is located at  $0.17$  eV lower, and its intensity is smaller than the QSGW. These properties imply that the QSGW may enhance the instability to the JT dis-

TABLE I. Total and atomic magnetic moments in  $\mu_B/\text{f.u.}$  and  $\mu_B$ , respectively. The experimental values for the austenite and martensite phases are in the upper and lower rows of the right column, respectively. Extrapolation with the Stoner model evaluated these values on austenite phases ( $M_{\text{ex},0}$ ). See text for details.

$c/a$	QSGW				GGA+ $U$				GGA				Expt.	
	Mn	Ni	Ga	Total	Mn	Ni	Ga	Total	Mn	Ni	Ga	Total	Total	
1.00	3.56	0.61	-0.03	4.74	3.82	0.32	-0.05	4.41	3.42	0.36	-0.05	4.09	4.53 [58],	4.28 [59],
1.10	3.55	0.62	-0.03	4.76	3.82	0.39	-0.05	4.54	3.42	0.43	-0.05	4.23	4.26 [60]	
1.20	3.50	0.59	-0.04	4.63	3.80	0.40	-0.06	4.53	3.37	0.44	-0.05	4.20	4.23 [58],	4.16 [59],
1.25	3.44	0.55	-0.04	4.49	3.78	0.37	-0.06	4.44	3.35	0.43	-0.06	4.13	4.04 [60],	4.17 [48]

tortion more than GGA (or GGA +  $U$ ). We also observed a similarity between GGA and GGA +  $U$  on that peak. This is because its electronic states are not formed by the Mn 3d orbitals. Details will be discussed in Sec. III D.

The other important result of focus is an unoccupied state at about 2 eV in the minority spin state in all cases of  $c/a$ . This state is identified as the upper state of exchange splitting. Compared to GGA, QSGW evaluates its location as about 0.4 eV higher. This result can be understood as an underestimation of orbital energy in the GGA calculation. The corresponding peak of GGA +  $U$  is rather close to the peak position of QSGW.

Depending on  $c/a$ , the resemblance of GGA +  $U$  and QSGW in the DOS at the Fermi level is altered (see insets of Fig. 2). Since QSGW explicitly incorporates the electron localization effect, this change suggests that the theoretical model for describing electron correlations, including the choice of parameters ( $U$ ), should differ depending on structural parameters ( $c/a$ ). In particular, for  $c/a = 1.20$ , the DOS peak on the Fermi level observed in GGA disappears in QSGW and GGA +  $U$ . A coincidence of DOS between GGA +  $U$  and QSGW appears near the Fermi level in the tetragonal phase; for example, the peak position shifted to the unoccupied side ( $\sim 0.15$  eV, see Sec. III D) and the values of DOS and its slope at the Fermi level. This finding implies that the electron localization effect included in QSGW could be reproduced by the + $U$  correction in GGA (GGA +  $U$ ).

### C. Magnetic moments

Table I shows the total and atomic magnetic moments. The total magnetic moment mainly originates from the Mn atom, while the Ga atom has a small opposite moment to Mn and Ni. The total magnetic moment obtained from the GGA calculations agrees with those reported in a previous theoretical study: 4.11 and 4.14  $\mu_B/\text{f.u.}$  for the cubic ( $c/a = 1.00$ ) and tetragonal ( $c/a = 1.25$ ) phases, respectively [30]. Comparing the results of  $c/a = 1.25$  with those of  $c/a = 1.00$ , we also observed that although the magnetic moment of Mn decreased for all methods, the magnetic moment of Ni showed a different trend, namely, a decrease in QSGW and an increase in both GGA and GGA +  $U$ . In the two latter cases, as  $c/a$  increases, the total magnetic moment initially increases, then decreases, and finally becomes almost the same for  $c/a = 1.00$  and 1.25. This trend was also shown in the previous study of GGA +  $U$  [65].

Previous experimental results by Ooiwa *et al.* [58] suggested that the Stoner model [66] ( $M_{\text{ex},T}^2 = M_{\text{ex},0}^2[1 - (T/\theta)^2]$ , where  $M_{\text{ex},T}$  is the magnetic moment at temperature  $T$ , and  $\theta$  is the Curie temperature) is valid below 300 K. Therefore, they used this model to determine the magnetic moment ( $M_{\text{ex},0}$ ) of the austenite phase by extrapolating it to zero temperature. Table I shows the results obtained using the same method for the experimental data in Refs. [59] (data below 300 K) and [60] (data below 270 K) to estimate the magnetic moment ( $M_{\text{ex},0}$ ) in the austenite phase. The magnetic moment of the martensitic phase (at nearly zero temperature) is suppressed compared to the austenite phase, specifically, by 0.30(=4.53-4.23), 0.12(=4.28-4.16), and 0.22(=4.26-4.04)  $\mu_B/\text{f.u.}$  in Refs. [58], [59], and [60], respectively. Such a property on the magnetic moment is also observed in QSGW, with a decrease of 0.11(=4.74-4.63) and 0.25(=4.74-4.49)  $\mu_B/\text{f.u.}$  for  $c/a = 1.20$  and 1.25, respectively. According to the values of atomic magnetic moment, the suppression is attributed to the Mn and Ni atoms. A similar trend in suppression was also reported in meta-GGA calculation with a suppression of 0.09  $\mu_B/\text{f.u.}$  (4.17 and 4.08  $\mu_B/\text{f.u.}$  for the cubic and tetragonal phases, respectively) in SCAN -  $U$  (1.8 eV) [30] and, however, is never seen in GGA and GGA +  $U$ , as shown in Table I. Assuming QSGW or meta-GGA includes an important amount of electron localization effect, the larger magnetic moment may indicate evidence of larger strength on electron localization in the cubic phase.

Although  $c/a$  dependence of magnetic moment on QSGW is consistent with experimental trends, the value of the moment is overestimated compared to the GGA and experiments (Table I). A tendency for magnetic moment overestimation has been reported in the QSGW approach [40,45]. Meanwhile, the GGA often underestimates the magnetic moment in localized electron systems due to the underestimation of exchange splitting in GGA. QSGW can slightly overcompensate for such an underestimation, giving a much larger magnetic moment than GGA. Unlike GGA, GGA +  $U$  can compensate for such an underestimation by the  $U$  parameter, yielding a larger value, as shown in Table I.

QSGW is able to incorporate electron charge fluctuation effects through screened Coulomb matrix but not spin fluctuation effects. It has been pointed out that such a neglecting of spin fluctuation leads to an overestimation of magnetic moment in fcc-Ni metal compared to the experimental values [45]. The overestimation in the magnetic moment by QSGW in this work may be due to the same reason. This problem is possibly overcome by including the spin fluctuation effect in the GW scheme [67].

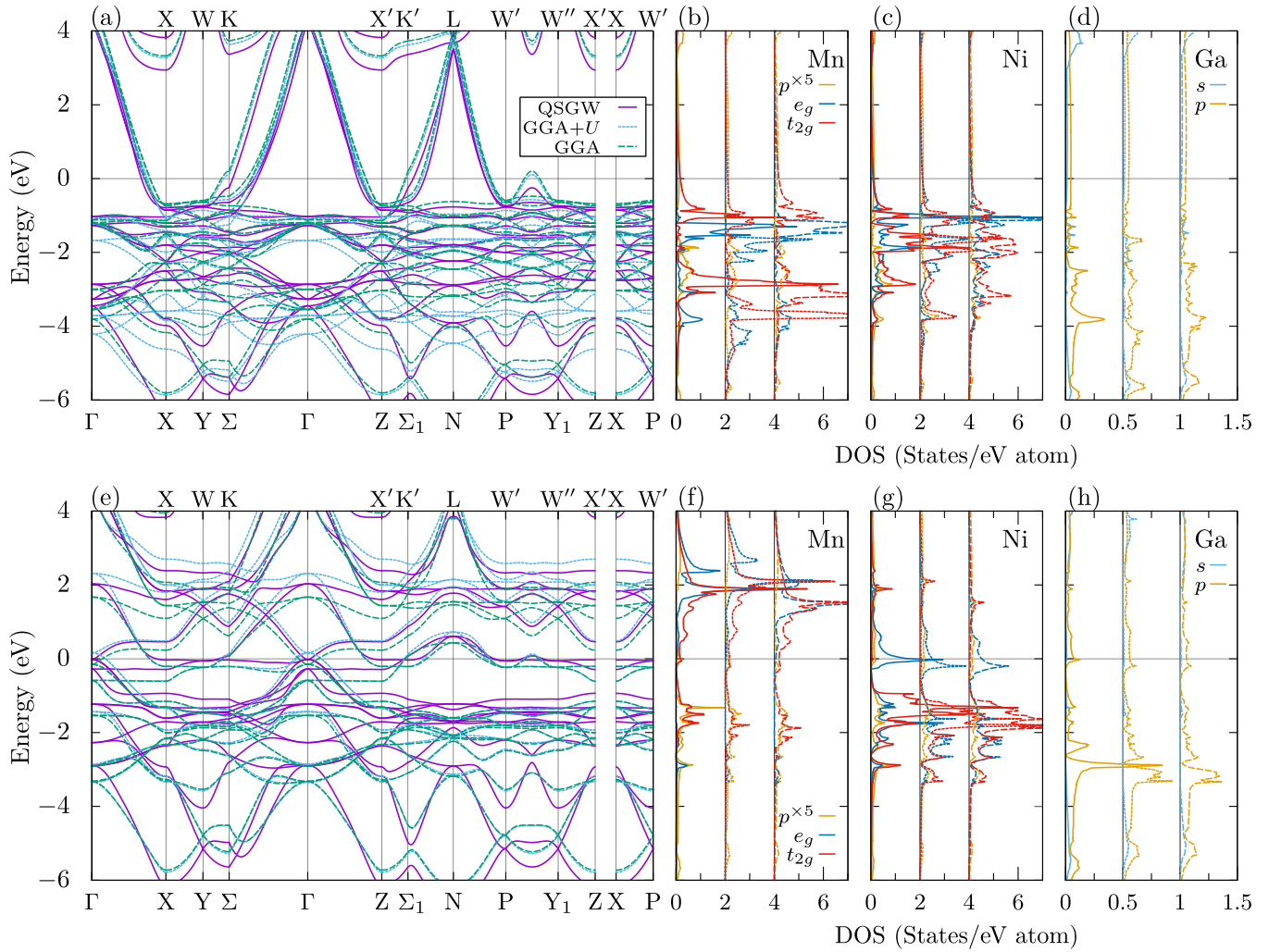


FIG. 3. Band dispersion curves (a) and PDOS (b)–(d) of the majority spin state at  $c/a = 1.00$  with QSGW (solid lines), GGA +  $U$  (dotted lines), and GGA (dashed lines). Similarly, band dispersion curves (e) and PDOS (f)–(h) of the minority spin state. The symbols in the upper horizontal axis (a), (e) are the corresponding fcc  $k$  points. The origin of PDOS for GGA +  $U$  (GGA) data is set to the level of 2.0 (4.0) states/eV atom for Mn and Ni, and 0.5 (1.0) states/eV atom for Ga. The  $p$  orbital components of Mn and Ni are exaggerated by five times.

#### D. Band dispersion curves and partial density of states

Figures 3 and 4, shows the dispersion curves and partial density of states (PDOS) at  $c/a = 1.00$ . The dispersions are plotted along the symmetry lines of the first BZ shown in Fig. 1(b). Note that, in the case of  $c/a = 1.00$ , the energy eigenvalues on the specific  $k$  points degenerate due to symmetry, such as at the X and Z or Y and P points. This redundant presentation is to make the comparison with the tetragonal system clearer. The  $p$ -orbital-like states, characterized by large dispersion, cross the Fermi level in the majority spin state [Fig. 3(a)], whereas dispersionless states appear in the vicinity of the Fermi level for the minority spin state [Fig. 3(e)]. The dispersionless states, substantially consisting of nonbonding orbitals, contribute a peak structure in the DOS near the Fermi level. These states mainly comprise the Ni minority spin state  $e_g$  ( $d_{x^2-y^2}$ ,  $d_{3z^2-r^2}$ ) orbitals, while the  $t_{2g}$  ( $d_{xy}$ ,  $d_{yz}$ ,  $d_{zx}$ ) orbitals are almost occupied.

Compared with GGA, the  $d$  bandwidth is narrower, but the  $p$  bandwidth (around  $-5$  eV) is broader in QSGW. This property is a general trend of QSGW that has been pointed

out in previous studies [68]. In this comparison, a decrease of QSGW in the  $d$  bandwidth comes from a consequence of the intensely overscreened exchange interaction of GGA. The latter overscreened nature is based on the uniform electron gas model, in which the delocalization of electron wave function is inherently introduced.

From the difference between GGA and GGA +  $U$  in Figs. 3(a) and 3(e), the + $U$  correction shifts the occupied majority spin states to lower energies and pushes the unoccupied minority spin states to higher energies. As a result, the minority spin states below the Fermi level are insignificantly affected by + $U$ . The  $d$  orbitals of QSGW in the minority spin state are generally shifted to higher energies than that of GGA. The underestimation of exchange splitting in GGA, as pointed out in the previous section (Sec. III C), is clearly observed.

Figure 4 shows the band dispersion curves and PDOS at  $c/a = 1.20$  in the same form as Fig. 3. Because of the distortion to the tetragonal cell, the symmetry is reduced from the cubic phase; thus,  $t_{2g}$  separates into  $e'_g$  ( $d_{yz}$ ,  $d_{zx}$ ) and  $b_{2g}$  ( $d_{xy}$ ) orbitals, and  $e_g$  separates into  $a_{1g}$  ( $d_{3z^2-r^2}$ ) and  $b_{1g}$  ( $d_{x^2-y^2}$ )

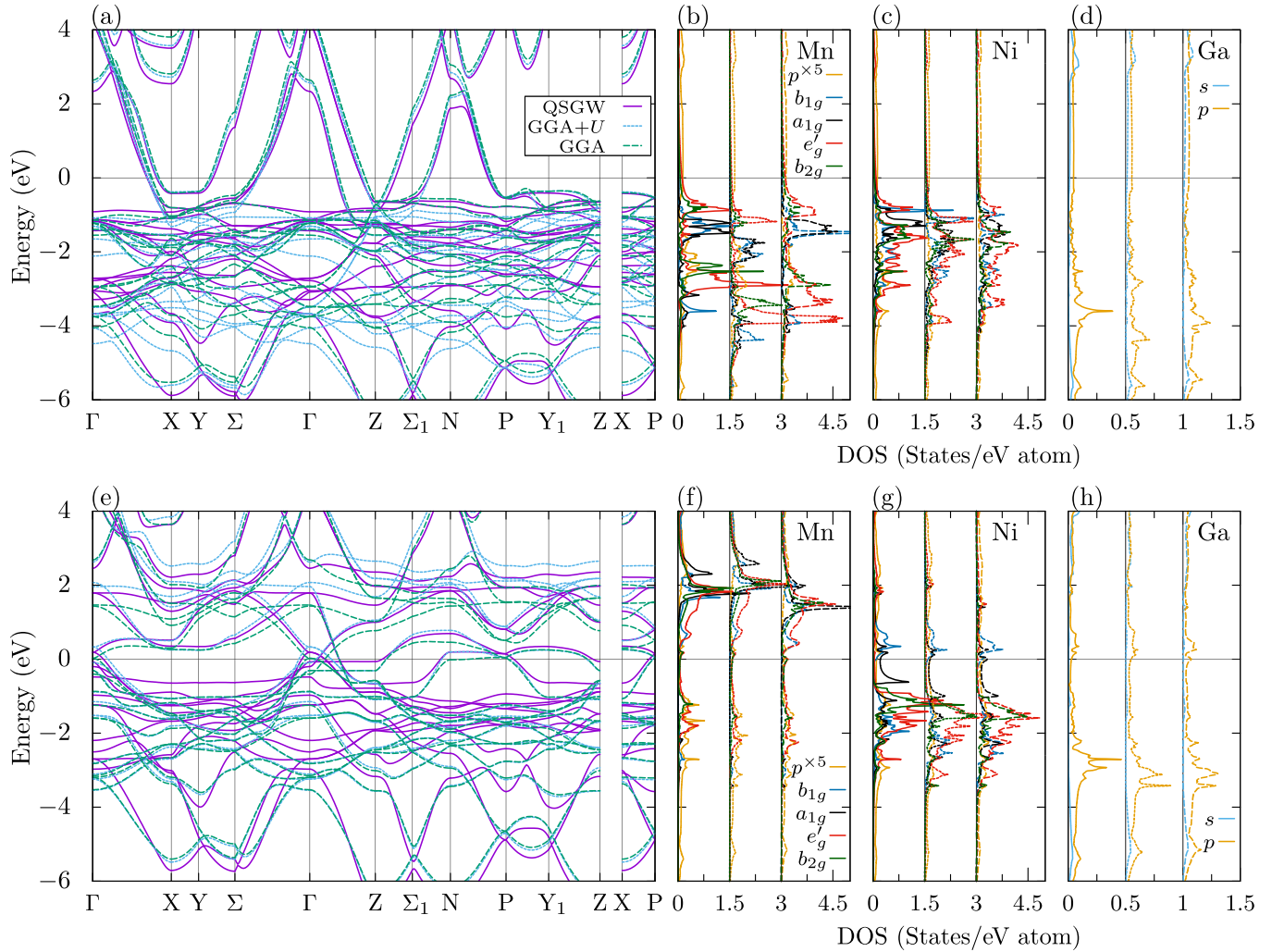


FIG. 4. Band dispersion curves (a) and PDOS (b)–(d) of the majority spin state at  $c/a = 1.20$  with QSGW (solid lines), GGA +  $U$  (dotted lines), and GGA (dashed lines). Similarly, band dispersion curves (e) and PDOS (f)–(h) of the minority spin state. The origin of PDOS for GGA +  $U$  (GGA) data is set to the level of 1.5 (3.0) states/eV atom for Mn and Ni, and 0.5 (1.0) states/eV atom for Ga. The  $p$  orbital components of Mn and Ni are exaggerated by five times.

orbitals. The Ni  $d_{3z^2-r^2}$  orbital close to the Fermi level in the cubic phase moves to below the Fermi level while the  $d_{x^2-y^2}$  moves to above the Fermi level, stabilizing the tetragonal crystal structure due to the band JT effect. The dispersionless states on the minority spin state at the N-P line in the first BZ just above the Fermi level form a van Hove singularity, and a corresponding peak in DOS is mainly observed as the Ni  $a_{1g}$  orbital. These features are exhibited in all of the present methods, but there are some differences, e.g., the states on the N-P line described above cross the Fermi level in GGA but locate about 0.15 eV above the Fermi level in QSGW and GGA +  $U$ . We speculate that such an electronic state may induce further structural instability. For example, GGA has slightly overestimated the optimized  $c/a$  (1.25 in Ref. [30], 1.26 in Ref. [69]) compared to the experimental value ( $c/a = 1.20$ ). Indeed, Zelený *et al.* have shown that the modulated long-period structures such as 4O, 10M, and 14M are more stable than the NM structure by GGA and GGA +  $U$  calculations [31,32]. In such modulated structures,

translational symmetry in the  $z$  direction is broken at the twin boundary, changing the level of Ni  $a_{1g}$  orbital and possibly forming orbital hybridization with the neighboring atoms.

Along with the N-P line, we found a similar state along the  $\Gamma$ -Z line in the minority spin state, appearing around  $-0.16$  eV in GGA, while a state with a flat dispersion close to the Fermi level appears in QSGW. The direction to the Z point from the  $\Gamma$  point in the first BZ corresponds to the  $z$  direction shown in Fig. 1. The main contribution to this state is the Ni  $d_{x^2-y^2}$  orbital, which is a nonbonding orbital toward Ni-Ni in the  $xy$  plane. This state comes from the part of the  $d_{x^2-y^2}$  orbital that does not significantly move to higher energy by the band JT effect. This state appears only in one-dimensional regions on the  $\Gamma$ -Z line and does not contribute so much to DOS. Therefore, it hardly affects electronic instability.

As described in the Secs. III B and III D, there are non-negligible electronic structure differences between QSGW and GGA. It is found that some of these differences

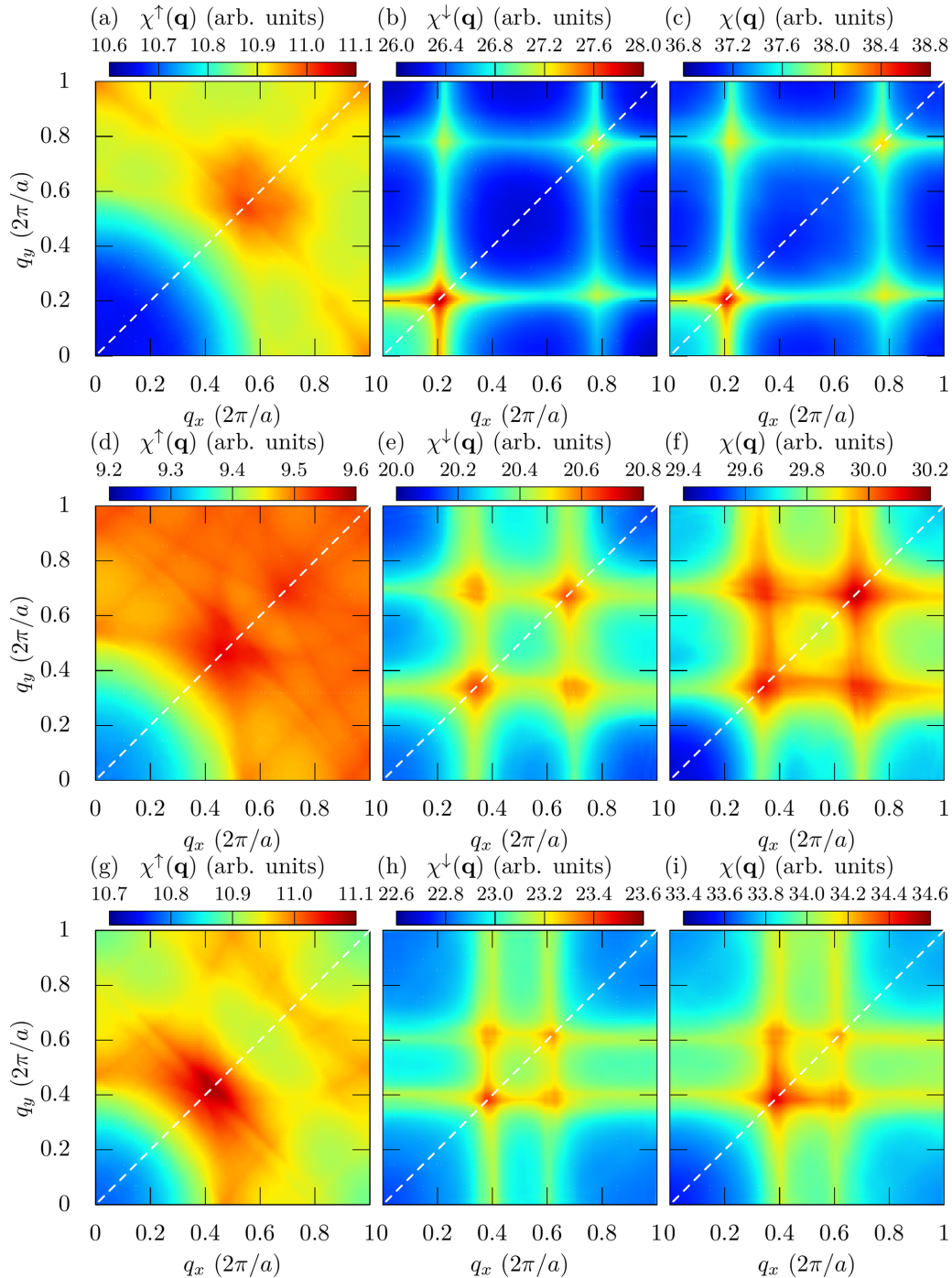


FIG. 5. Generalized susceptibility of the majority spin (a), the minority spin (b), and the total (c) with QSGW, (d)–(f) with GGA +  $U$ , and (g)–(i) with GGA. White dashed lines represent the [110] directions.

with QSGW become smaller by introducing + $U$  (1.8 eV). However, especially in the cubic phase, a noteworthy difference remains within the vicinity of the Fermi level between QSGW and GGA +  $U$ . To reproduce an electronic structure close to that of QSGW by conventional DFT, one of the possible ways is to employ a few parameters of electron correlation, such as Hubbard  $U$  and Hund's  $J$ , appropriately [70]. In such cases, the QSGW may provide a guide for identifying these parameters. Once the parameters are determined, it is

possible to utilize the virtues of the conventional DFT approach (total energy, structural optimization, reasonable computational cost, etc.).

### E. Generalized susceptibility

Figure 5 shows the distribution of  $\chi^\rho(\mathbf{q})$  ( $\rho = \uparrow, \downarrow$ ) and  $\chi(\mathbf{q}) = \chi^\uparrow(\mathbf{q}) + \chi^\downarrow(\mathbf{q})$  of the cubic phase in the  $q_z = 0$  plane. The minority spin component ( $\rho = \downarrow$ ) has a domi-

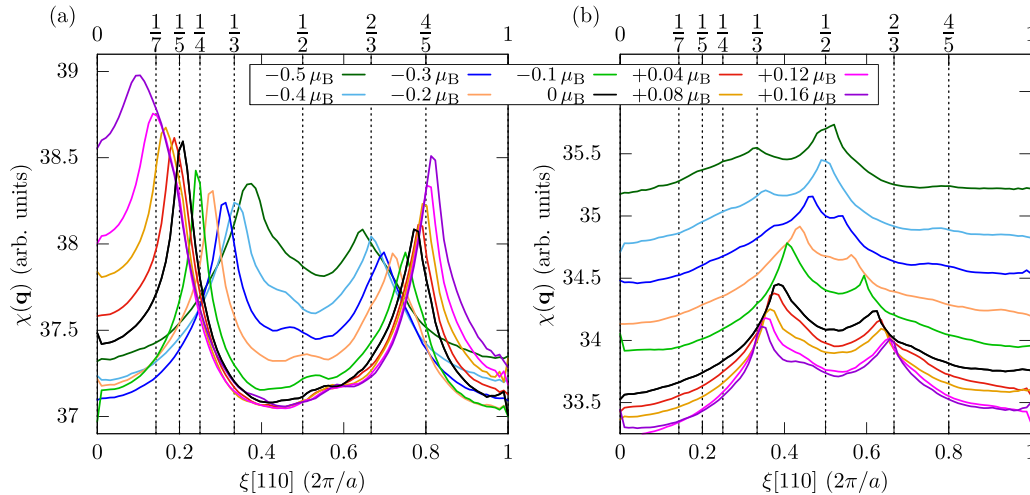


FIG. 6. Magnetic moment dependence of generalized susceptibility by (a) QSGW and (b) GGA.

nant contribution, and the overall  $\mathbf{q}$  dependence originates from the minority spin component due to a large number of states around the Fermi level. In QSGW, there is a strong peak around  $\xi = 1/5$  ( $\mathbf{q} = (\xi, \xi, 0)2\pi/a$ ), as shown in Figs. 5(b) and 5(c). This  $\xi$  is supposed to be the nesting vector corresponding to five-period structures such as 10M. This theoretical result strongly suggests that the  $\text{Ni}_2\text{MnGa}$  possesses instability to the five-period structure known as the ground state. Note that it can be pointed out that a peak appears at  $\xi = 0.23$  in SCAN( $U = 0$ ) (Fig. 4. in Ref. [30]), which is slightly larger than  $1/5$ . Interestingly, the second substantial peak at  $\xi = 4/5$  can be assigned to a periodicity of 1.25 layers along the [110] direction.

In GGA [see Figs. 5(g)–5(i)], the first peak position shifts to a larger wave number, and the secondary peak shifts to a smaller wave number. The present GGA results agree with previous LDA/GGA results regarding the presence and position of two peaks in the [110] direction. For example, there are peaks at  $\xi = 0.38$  and  $0.62$  in Fig. 5(i), corresponding to  $\xi = 0.42$  and  $0.59$  in LDA [17],  $\xi = 0.39$  and  $0.60$  in GGA [30], respectively. Concerned about the peak around  $\xi = 0.4$ , we will discuss our GGA results in the second paragraph from the last of this section. As we discussed in Sec. III D, for  $c/a = 1.00$ , the states near the Fermi level predominantly consisting of Ni 3d orbitals are insensitive to the Mn's  $U$  parameter; GGA +  $U$  gives a result similar to that of GGA, accompanied by peaks at  $\xi = 0.34$  and  $0.67$ . There is a clear difference in intensity between the peaks for both QSGW and GGA cases. The peak corresponding to longer period structures (smaller  $\xi$ ) exceeds those of the others (larger  $\xi$ , corresponding to shorter period structures), as shown in Figs. 5(c) and 5(i). This difference in intensity suggests that the instability to the long-period structure is more substantial than that to the short-period structure, promoting the formation of long-period structures. In contrast, the largest peak appears at a larger  $\xi$  in GGA +  $U$  [Fig. 5(f)].

In experimental works, it has been found that a tiny replacement at the Ga site (Ga sublattice) with Mn atoms (an increase in the number of valence electrons) changes the modulated phase from 10M to 14M [14]. From the first-principles

CPA calculations, which include the mean-field effect, Q. Hu *et al.* have demonstrated that the Mn at Ga sites increases the atomic magnetic moments of Ni and Mn [26]. Specifically, according to their result, for an increase of 0.1 in the number of electrons per atom ( $\Delta n = 0.1 e/a = 0.4 e/f.u.$ ), the whole magnetic moment on Ni and Mn increases by  $0.1 \mu_B/f.u.$  This is due to the strengthening of the exchange interaction between the neighboring magnetic atoms. Note that if we employ a simple Fermi level shift to the higher-energy side, the magnetic moment decreases due to the occupation of a minority spin state. In order to clarify the behavior in the rigid-band approximation (RBA), we investigated the magnetic moment dependence of the generalized susceptibility under the fixed number of electrons ( $\Delta n = 0$ ).

Figure 6 shows the magnetic moment dependence of  $\chi$ . The results of QSGW clearly show the emergence of peaks at  $\xi = 1/7$ ,  $\xi = 1/5$ , and  $\xi = 1/3$ , corresponding to 14M, 10M, and 6M structures, respectively, depending on the subtle changes in the magnetic moment ( $\Delta m$ ). This emergence of the peaks indicates that the cubic electronic state inherently has instability to these modulated structures. In contrast, the GGA calculation shows that the nesting vector (peak position) is not only so insensitive to  $\Delta m$  but also out of the range of the 10M or 14M structure. Our QSGW result also shows that the nesting vector decreases (increases) with increasing (decreasing)  $\Delta m$ ; for example, the nesting vector of 10M ( $\Delta m = 0 \mu_B/f.u.$ ) shifts to that of 14M ( $\Delta m = +0.12 \mu_B/f.u.$ ) with an increase in the magnetic moment of  $0.12 \mu_B/f.u.$  This change in the magnetic moment almost corresponds to  $\Delta n = 0.1 e/a$  by referring to the theoretical results in Ref. [26]. Meanwhile, the 14M phase was experimentally observed at  $\Delta n = 0.11 e/a$  [61]. However, in our results based on RBA, the nesting vector increases with increasing  $\Delta n$  unless  $\Delta m$  increases (see Sec. III G). This result implies the following: an increase in the magnetic moment is necessary to reduce the nesting vector to  $\xi = 1/7$  (corresponding to 14M). In particular, since the Fermi surface of the minority spin state comprises Ni  $e_g$  orbitals, the Ni magnetic moment possibly plays a role in controlling the nesting vector.

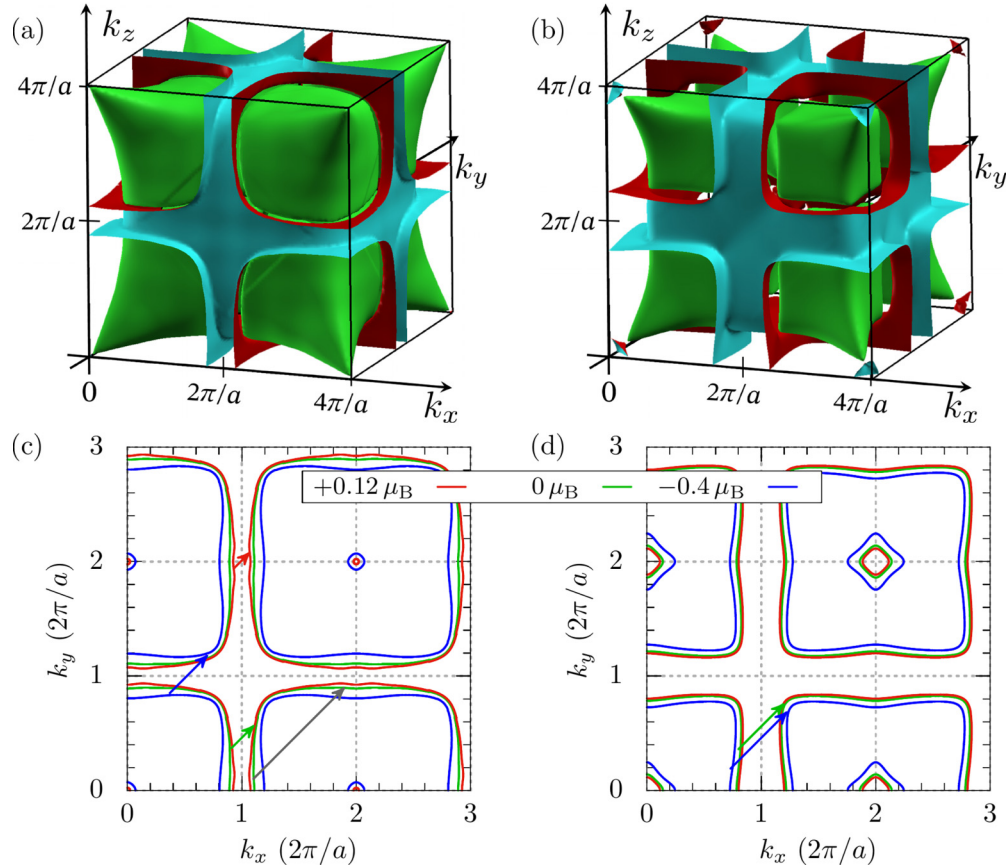


FIG. 7. Fermi surface of minority spin state in the extended BZ by (a) QSGW and (b) GGA. The  $\Gamma$  point corresponds to the corners and center of the cubic. Magnetic moment dependence of the Fermi surface for (c) QSGW and (d) GGA on the surface with  $k_z = 0$ . Red, green, blue, and gray arrows in (c) represent  $(1/7, 1/7)$ ,  $(1/5, 1/5)$ ,  $(1/3, 1/3)$ , and  $(4/5, 4/5)$  vectors, respectively. Green and blue vectors in (d) represent  $(2/5, 2/5)$  and  $(1/2, 1/2)$ , respectively.

As also shown in Fig. 6(a), in contrast with the first peak mentioned above, the peak around  $\xi = 4/5$  is less sensitive to magnetic moment changes. This peak can be involved with the double layers shuffling that appears in the 10M and 14M structures (see Sec. III H).

Effective couplings of interatomic exchange interaction should decrease at high temperatures due to the fluctuations of magnetic moment, which corresponds to a situation where the magnetic moment declines below the Curie temperature. There are double peaks at  $\xi = 1/3$  and  $\xi = 2/3$  in the case of  $\Delta m = -0.4 \mu_B/\text{f.u.}$ , which corresponds to the 6M structure. Note that the reason why  $\xi = 2/3$  promotes the 6M structure as well as  $\xi = 1/3$  was demonstrated in Ref. [71]. As shown in Figs. 5(g) and 5(h), both  $\chi^\uparrow$  and  $\chi^\downarrow$  have a peak around  $\xi = 0.4$  in GGA. According to the discussion in Ref. [19], the peak around  $\xi = 0.4$  has been considered to lead to the softening of phonon frequency in the [110] direction and to be an indication of a three-period structure. That work suggested that this non-negligible difference from  $\xi = 1/3$ , corresponding to a nesting vector for a three-period structure, might be corrected by considering the suppression of magnetic moment caused by temperature effects: the peak position of  $\chi^\uparrow$  tends to move to  $\xi = 1/3$ . We obtained a similar tendency from our GGA results (not shown here). However, in our  $\chi$  [Fig. 6(b)], the largest peak appears around  $\xi = 1/2$  at  $\Delta m = -0.4 \mu_B/\text{f.u.}$  due to the contribution of  $\chi^\downarrow$ .

In summary of this section, the  $\chi$  of QSGW is highly sensitive to magnetic moment changes: the peak position ( $\xi = 1/7, 1/5, 1/4, 1/3$ , etc.) varies with the moment (see also Sec. III G). The presence of peaks over such a wide range is not shown in the GGA calculation. It is interesting to note that the four-period structure, corresponding to  $\xi = 1/4$ , has experimentally been reported in a Ni-Mn-Sn alloy [72]. The relationship to our result may be a future problem.

### F. Fermi surface

The properties of  $\chi$  and its magnetic moment dependence can be understood from the Fermi surface of the minority spin state shown in Fig. 7. This Fermi surface consists of two bands, which are mainly contributed from the Ni  $e_g$  orbitals. Our result by GGA [Fig. 7(b)] is in good agreement with those of previous studies [17,30,73], while QSGW [Fig. 7(a)] results in a larger Fermi surface. Figs. 7(c) and 7(d) show a cross-section of the Fermi surface at the  $k_z = 0$  plane. According to these results, the Fermi surface forms a squarelike shape centered at the  $\Gamma$  point. As indicated by arrows in Figs. 7(c) and 7(d), the connections to the surface belonging to the adjacent  $\Gamma$  points contribute to Fermi surface nesting. The square of QSGW is more spacious than that of GGA. Consequently, the QSGW gives a shorter nesting vector than the GGA. These squares on QSGW remarkably expand (shrink) with a

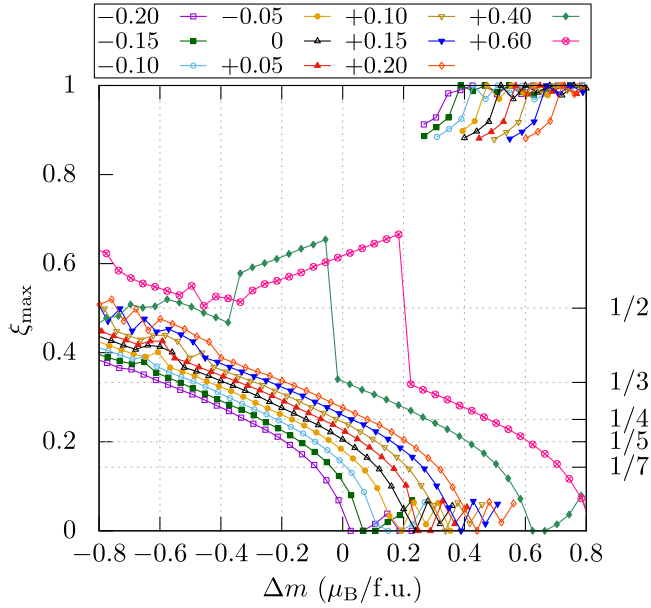


FIG. 8. Magnetization dependence of the nesting vectors for the  $\Delta n$  (e/f.u.) listed in the legend. Neighboring data are connected by lines for a guide to the eye, but some of them are not displayed to make the graph clear.

subtle increase (decrease) in the magnetic moment, as shown in Fig. 7(c), due to the existence of dispersionless minority spin states much close to the Fermi level. Thus, the peak of  $\chi$  appears at  $\xi = 1/7, 1/5$ , and  $1/3$  along the sequence of magnetic moment magnitudes.

### G. Nesting vectors

From Fig. 6, it is identified to assign maximum peak positions of  $\chi$  to  $\xi_{\max}$  for a magnetization. Figure 8 shows the data plot in the magnetization ( $\Delta m$ ) vs.  $\xi_{\max}$  by QSGW for several typical  $\Delta n$ 's within the RBA. Although in this approximation, the self-consistent fields expected from both  $\Delta n$  and  $\Delta m$  are not considered, the plot may indicate an occurrence of possible instability. As a general trend, the  $\xi_{\max}$  at the negative  $\Delta m$  decreases to zero and then jumps to larger values ( $\xi_{\max} \sim 1$ ) as the  $\Delta m$  increases. This jump is caused by a reversal of intensities between the two peaks of  $\chi$  shown in Fig. 6(a). An increase in the  $\Delta n$  leads to an increase in  $\xi_{\max}$ , indicating a suppression of long-period structural instability. In the small  $\xi_{\max}$  region, its change for the  $\Delta m$  or  $\Delta n$  is significant. A slight reduction in the number of electrons, for example, corresponding to Mn-site substitution by Cr [74,75], favors an instability to longer period structures. In such an instability, its period increases as  $\xi_{\max}$  decreases and eventually reaches infinity at  $\xi_{\max} = 0$ . This behavior corresponds to the appearance of the NM structure. In this sense, the NM structure can be attributed to a region where  $\xi_{\max}$  is close to zero. In Fig. 8, it is assigned to a region of positive  $\Delta m$ , although its weakly oscillating behavior appears along the horizontal axis due to the insufficient numerical accuracy of  $\xi_{\max} = 0$ . In the case of large positive  $\Delta n$  or large negative  $\Delta m$ , the  $\xi_{\max}$  approaches  $1/2$  associating with two-period structures such as 4O.

The CDW state is usually discussed with a nesting vector. For example, in  $\text{Ni}_2\text{MnGa}$ , some experimental groups have proposed possible nesting vectors of  $\xi = 0.46, 0.43$  [24,76], based on their results. These authors implied that their nesting vectors coincide with those of LDA/GGA. This is true in our data [Fig. 6(b)], and however, the nesting vector corresponding to those of the experiments does not appear in the QSGW results of  $\xi$  [Fig. 6(a)]. In Fig. 8, it can appear at large negative  $\Delta m$ .

### H. Nanotwin boundary alignment

The peak around  $\xi = 4/5$  clearly appears at the self-consistently determined state ( $\Delta m = 0 \mu_B$ ), as shown in Fig. 6(a). Its peak location is relatively insensitive to the effect of magnetic moment changes. This peak, whose strength is slightly smaller than those of the peaks around  $\xi = 1/7$  or  $1/5$ , possibly gives an implication of another instability in the system. The corresponding wavelength expected to be stabilized in the system may assign to 1.25 period (2.5M) along the [110] direction in real space when introducing the same ansatz as for the seven-period (14M) or five-period (10M). Since a lattice modulation with the wavelength corresponding to such periods is incommensurate, the lattice elastic energy may increase even though simultaneous structural relaxation is caused. According to such speculation, it is meaningful to suppose the existence of double-well potential among the layers, as shown in Fig. 9(a).

As a result, the 3-2 layer and 2-3 layer may become transferable to each other. This transfer means a kinetic motion of the nanotwin boundary in the martensitic phases. At the finite temperatures that such transfer is expected to appear, the kinetic motion may pass by a local transition state of layer configuration such as a 2-2 layer or a 3-3 layer, as depicted in Fig. 9(b). Energetics of the configurations containing a 2-2 layer or 3-3 layer is interesting so that the mechanism of the nanotwin boundary shift on martensitic transformation can be related to the electronic structure. In the present context, the local structure of a 2-2 layer or 3-3 layer means the transition state in the kinetic motion of the nanotwin boundary. We have to note that the solid system of a 2-2 layer or 3-3 layer periodicity has theoretically been discussed as a candidate for stable structures or a fluctuation of lattice distortion [31].

All of the above discussions based on generalized susceptibility are of instability in the electronic structure for the cubic (austenite) phase. Stability discussions of martensite phases are required in a physical accuracy comparable to the QSGW approach. Creation and annihilation of the nanotwin boundary associated with its kinetic motion are also interesting in the phase transition among the martensite phases of 10M, 14M, and NM.

## IV. SUMMARY

We investigated the electronic structure and magnetic moment of the cubic and tetragonal phases of ferromagnetic shape memory alloy  $\text{Ni}_2\text{MnGa}$  by the QSGW method. There is a large DOS at the Fermi level in the cubic phase ( $c/a = 1.00$ ) consisting of Ni  $e_g$  orbitals of minority spin state,

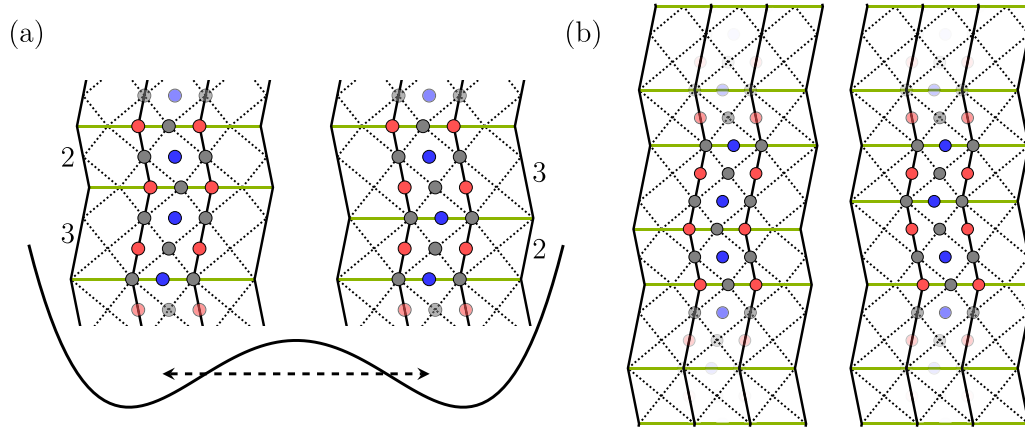


FIG. 9. Schematic illustration of modulated structures with nanotwin boundaries represented by green horizontal lines. (a) The double-well potential formed among nanotwin boundary alignments. (b) The 10M structure (left) and the structure after the nanotwin boundary shifts by an atomic layer (right). The red, blue, and gray spheres represent the Ga, Mn, and Ni atoms.

apparently suggesting structural instability due to the band JT effect. Such electronic structures near the Fermi level were insensitive to the  $U$  parameter of Mn and were not well described by the present GGA +  $U$  calculation. In the tetragonal phase ( $c/a = 1.20$ ), we found the peculiar electronic states that may destabilize the NM structure; the van Hove singularity and dispersionless state near the Fermi level. For both the cubic and tetragonal phases, the QSGW calculation shows the narrower bandwidth for the  $d$  orbitals than the GGA calculation and higher-energy levels of unoccupied orbital in the minority spin state, implying that the QSGW evaluates a stronger exchange interaction than the GGA. From the susceptibility analysis, we found that the electronic structure of the cubic phase inherently has the instability induced by the Fermi surface nesting to modulated structures of 10M and 14M as well as 6M. These instabilities were also found to be sensitive to the magnetic moment. This work will pave the way for a basic understanding of martensite phase transitions and give new foundations for the

theoretical/computational materials design to magnetic shape memory alloys.

#### ACKNOWLEDGMENTS

The authors (T.O. and M.O.) thank Ladislav Kalvoda, Petr Sedlák, Hanuš Seiner, Tomáš Koubský, Jaroslava Jakoubková, Tomosato Kanagawa, Jakub Luštinec, Martin Zelený, and Oleg Heczko for initiating the fascination in ferromagnetic shape memory alloy. The computation in this work was partly performed using the facilities of the Supercomputer Center, Institute for Solid State Physics (ISSP), The University of Tokyo, Japan. This work was partly supported by Japan Society for the Promotion of Science KAKENHI, Grant-in-Aid for Scientific Research (No. 21K04864 and No. 21KK0083). The crystal structure and Fermi surface illustrations were produced using VESTA [77] and XCrySDen [78]. The authors (T.O. and M.O.) acknowledge the SANTO project at Kanazawa University.

- [1] K. Ullakko, J. K. Huang, C. Kantner, R. C. O'Handley, and V. V. Kokorin, Large magnetic-field-induced strains in  $\text{Ni}_2\text{MnGa}$  single crystals, *Appl. Phys. Lett.* **69**, 1966 (1996).
- [2] A. Sozinov, A. A. Likhachev, N. Lanska, and K. Ullakko, Giant magnetic-field-induced strain in  $\text{NiMnGa}$  seven-layered martensitic phase, *Appl. Phys. Lett.* **80**, 1746 (2002).
- [3] O. Heczko, V. Kopecký, A. Sozinov, and L. Straka, Magnetic shape memory effect at 1.7 K, *Appl. Phys. Lett.* **103**, 072405 (2013).
- [4] A. Sozinov, N. Lanska, A. Soroka, and W. Zou, 12% magnetic field-induced strain in Ni-Mn-Ga-based non-modulated martensite, *Appl. Phys. Lett.* **102**, 021902 (2013).
- [5] O. Heczko, Magnetic shape memory effect and highly mobile twin boundaries, *Mater. Sci. Technol.* **30**, 1559 (2014).
- [6] F.-x. Hu, B.-g. Shen, J.-r. Sun, and G.-h. Wu, Large magnetic entropy change in a Heusler alloy  $\text{Ni}_{52.6}\text{Mn}_{23.1}\text{Ga}_{24.3}$  single crystal, *Phys. Rev. B* **64**, 132412 (2001).
- [7] A. Planes, L. Mañosa, and M. Acet, Magnetocaloric effect and its relation to shape-memory properties in ferromagnetic Heusler alloys, *J. Phys.: Condens. Matter* **21**, 233201 (2009).
- [8] N. Sarawate and M. Dapino, Experimental characterization of the sensor effect in ferromagnetic shape memory Ni-Mn-Ga, *Appl. Phys. Lett.* **88**, 121923 (2006).
- [9] V. V. Khovaylo, K. P. Skokov, Y. S. Koshkid'ko, V. V. Koledov, V. G. Shavrov, V. D. Buchelnikov, S. V. Taskaev, H. Miki, T. Takagi, and A. N. Vasiliev, Adiabatic temperature change at first-order magnetic phase transitions:  $\text{Ni}_{2.19}\text{Mn}_{0.81}\text{Ga}$  as a case study, *Phys. Rev. B* **78**, 060403(R) (2008).
- [10] L. Righi, F. Albertini, E. Villa, A. Paoluzi, G. Calestani, V. Chernenko, S. Besseghini, C. Ritter, and F. Passaretti, Crystal structure of 7M modulated Ni-Mn-Ga martensitic phase, *Acta Mater.* **56**, 4529 (2008).
- [11] L. Righi, F. Albertini, L. Pareti, A. Paoluzi, and G. Calestani, Commensurate and incommensurate "5M" modulated crystal

- structures in Ni-Mn-Ga martensitic phases, *Acta Mater.* **55**, 5237 (2007).
- [12] P. Entel, V. D. Buchelnikov, V. V. Khovailo, A. T. Zayak, W. A. Adeagbo, M. E. Gruner, H. C. Herper, and E. F. Wassermann, Modelling the phase diagram of magnetic shape memory Heusler alloys, *J. Phys. D* **39**, 865 (2006).
- [13] S. Kaufmann, U. K. Röbber, O. Heczko, M. Wuttig, J. Buschbeck, L. Schultz, and S. Fähler, Adaptive Modulations of Martensites, *Phys. Rev. Lett.* **104**, 145702 (2010).
- [14] N. Lanska, O. Söderberg, A. Sozinov, Y. Ge, K. Ullakko, and V. K. Lindroos, Composition and temperature dependence of the crystal structure of Ni-Mn-Ga alloys, *J. Appl. Phys.* **95**, 8074 (2004).
- [15] A. Zheludev, S. M. Shapiro, P. Wochner, A. Schwartz, M. Wall, and L. E. Tanner, Phonon anomaly, central peak, and microstructures in Ni<sub>2</sub>MnGa, *Phys. Rev. B* **51**, 11310 (1995).
- [16] S. Fujii, S. Ishida, and S. Asano, Electronic structure and lattice transformation in Ni<sub>2</sub>MnGa and Co<sub>2</sub>NbSn, *J. Phys. Soc. Jpn.* **58**, 3657 (1989).
- [17] O. Velikokhatnyi and I. Naumov, Electronic structure and instability of Ni<sub>2</sub>MnGa, *Phys. Solid State* **41**, 617 (1999).
- [18] V. V. Godlevsky and K. M. Rabe, Soft tetragonal distortions in ferromagnetic Ni<sub>2</sub>MnGa and related materials from first principles, *Phys. Rev. B* **63**, 134407 (2001).
- [19] Y. Lee, J. Y. Rhee, and B. N. Harmon, Generalized susceptibility of the magnetic shape-memory alloy Ni<sub>2</sub>MnGa, *Phys. Rev. B* **66**, 054424 (2002).
- [20] C. Bungaro, K. M. Rabe, and A. Dal Corso, First-principles study of lattice instabilities in ferromagnetic Ni<sub>2</sub>MnGa, *Phys. Rev. B* **68**, 134104 (2003).
- [21] A. T. Zayak, P. Entel, J. Enkovaara, A. Ayuela, and R. M. Nieminen, First-principles investigations of homogeneous lattice-distortive strain and shuffles in Ni<sub>2</sub>MnGa, *J. Phys.: Condens. Matter* **15**, 159 (2003).
- [22] S. Özdemir Kart, M. Uludoğan, I. Karaman, and T. Çağın, DFT studies on structure, mechanics and phase behavior of magnetic shape memory alloys: Ni<sub>2</sub>MnGa, *Phys. Status Solidi A* **205**, 1026 (2008).
- [23] M. Zelený, A. Sozinov, L. Straka, T. Björkman, and R. M. Nieminen, First-principles study of Co- and Cu-doped Ni<sub>2</sub>MnGa along the tetragonal deformation path, *Phys. Rev. B* **89**, 184103 (2014).
- [24] S. W. D'Souza, A. Rai, J. Nayak, M. Maniraj, R. S. Dhaka, S. R. Barman, D. L. Schlagel, T. A. Lograsso, and A. Chakrabarti, Coexistence of charge-density wave and ferromagnetism in Ni<sub>2</sub>MnGa, *Phys. Rev. B* **85**, 085123 (2012).
- [25] M. A. Uijttewaala, T. Hickel, J. Neugebauer, M. E. Gruner, and P. Entel, Understanding the Phase Transitions of the Ni<sub>2</sub>MnGa Magnetic Shape Memory System from First Principles, *Phys. Rev. Lett.* **102**, 035702 (2009).
- [26] Q.-M. Hu, C.-M. Li, S. E. Kulkova, R. Yang, B. Johansson, and L. Vitos, Magnetoelastic effects in Ni<sub>2</sub>Mn<sub>1+x</sub>Ga<sub>1-x</sub> alloys from first-principles calculations, *Phys. Rev. B* **81**, 064108 (2010).
- [27] B. Dutta, A. Çakır, C. Giacobbe, A. Al-Zubi, T. Hickel, M. Acet, and J. Neugebauer, *Ab initio* Prediction of Martensitic and Intermartensitic Phase Boundaries in Ni-Mn-Ga, *Phys. Rev. Lett.* **116**, 025503 (2016).
- [28] M. Zelený, L. Straka, A. Sozinov, and O. Heczko, *Ab initio* prediction of stable nanotwin double layers and 4O structure in Ni<sub>2</sub>MnGa, *Phys. Rev. B* **94**, 224108 (2016).
- [29] B. Himmetoglu, V. M. Katukuri, and M. Cococcioni, Origin of magnetic interactions and their influence on the structural properties of Ni<sub>2</sub>MnGa and related compounds, *J. Phys.: Condens. Matter* **24**, 185501 (2012).
- [30] D. R. Baigutlin, V. V. Sokolovskiy, O. N. Miroshkina, M. A. Zagrebin, J. Nokelainen, A. Pulkkinen, B. Barbiellini, K. Pussi, E. Lähderanta, V. D. Buchelnikov, and A. T. Zayak, Electronic structure beyond the generalized gradient approximation for Ni<sub>2</sub>MnGa, *Phys. Rev. B* **102**, 045127 (2020).
- [31] M. Zelený, L. Straka, A. Sozinov, and O. Heczko, Transformation paths from cubic to low-symmetry structures in Heusler Ni<sub>2</sub>MnGa compound, *Sci. Rep.* **8**, 7275 (2018).
- [32] M. Zelený, P. Sedlák, O. Heczko, H. Seiner, P. Vertát, M. Obata, T. Kotani, T. Oda, and L. Straka, Effect of electron localization in theoretical design of Ni-Mn-Ga based magnetic shape memory alloys, *Mater. Des.* **209**, 109917 (2021).
- [33] T. Koubský, P. Sedlák, H. Seiner, J. Fojtřková, M. Obata, T. Oda, and L. Kalvoda, *Ab initio* study of martensitic transition in Ni<sub>2</sub>MnGa, *Acta Phys. Pol. A* **134**, 804 (2018).
- [34] S. V. Faleev, M. van Schilfgaarde, and T. Kotani, All-Electron Self-Consistent GW Approximation: Application to Si, MnO, and NiO, *Phys. Rev. Lett.* **93**, 126406 (2004).
- [35] M. van Schilfgaarde, T. Kotani, and S. Faleev, Quasiparticle Self-Consistent GW Theory, *Phys. Rev. Lett.* **96**, 226402 (2006).
- [36] T. Kotani, M. van Schilfgaarde, and S. V. Faleev, Quasiparticle self-consistent GW method: A basis for the independent-particle approximation, *Phys. Rev. B* **76**, 165106 (2007).
- [37] L. Hedin, New method for calculating the one-particle Green's function with application to the electron-gas problem, *Phys. Rev.* **139**, A796 (1965).
- [38] D. Deguchi, K. Sato, H. Kino, and T. Kotani, Accurate energy bands calculated by the hybrid quasiparticle self-consistent GW method implemented in the ecalj package, *Jpn. J. Appl. Phys.* **55**, 051201 (2016).
- [39] H. Sakakibara, T. Kotani, M. Obata, and T. Oda, Finite electric-field approach to evaluate the vertex correction for the screened Coulomb interaction in the quasiparticle self-consistent GW method, *Phys. Rev. B* **101**, 205120 (2020).
- [40] H. Okumura, K. Sato, and T. Kotani, Spin-wave dispersion of 3d ferromagnets based on quasiparticle self-consistent GW calculations, *Phys. Rev. B* **100**, 054419 (2019).
- [41] H. Yoon, S. W. Jang, J. H. Sim, T. Kotani, and M. J. Han, Magnetic force theory combined with quasi-particle self-consistent GW method, *J. Phys.: Condens. Matter* **31**, 405503 (2019).
- [42] Y. Lee, T. Kotani, and L. Ke, Role of nonlocality in exchange correlation for magnetic two-dimensional van der Waals materials, *Phys. Rev. B* **101**, 241409(R) (2020).
- [43] M. S. Hybertsen and S. G. Louie, Electron correlation in semiconductors and insulators: Band gaps and quasiparticle energies, *Phys. Rev. B* **34**, 5390 (1986).
- [44] L. Y. Isseroff and E. A. Carter, Importance of reference Hamiltonians containing exact exchange for accurate one-shot GW calculations of Cu<sub>2</sub>O, *Phys. Rev. B* **85**, 235142 (2012).
- [45] L. Sponza, P. Pisanti, A. Vishina, D. Pashov, C. Weber, M. van Schilfgaarde, S. Acharya, J. Vidal, and G. Kotliar, Self-energies in itinerant magnets: A focus on Fe and Ni, *Phys. Rev. B* **95**, 041112(R) (2017).
- [46] T. Kotani and M. van Schilfgaarde, Spin wave dispersion based on the quasiparticle self-consistent GW method: NiO,

- MnO and  $\alpha$ -MnAs, *J. Phys.: Condens. Matter* **20**, 295214 (2008).
- [47] S. A. Chambers, T. Droubay, T. C. Kaspar, M. Gutowski, and M. van Schilfhaarde, Accurate valence band maximum determination for SrTiO<sub>3</sub>(001), *Surf. Sci.* **554**, 81 (2004).
- [48] P. J. Webster, K. R. Ziebeck, S. L. Town, and M. S. Peak, Magnetic order and phase transformation in Ni<sub>2</sub>MnGa, *Philos. Mag. B* **49**, 295 (1984).
- [49] P. Sedláč, H. Seiner, L. Bodnárová, O. Heczko, and M. Landa, Elastic constants of non-modulated Ni-Mn-Ga martensite, *Scr. Mater.* **136**, 20 (2017).
- [50] V. A. Chernenko, C. Seguí, E. Cesari, J. Pons, and V. V. Kokorin, Sequence of martensitic transformations in Ni-Mn-Ga alloys, *Phys. Rev. B* **57**, 2659 (1998).
- [51] T. Kotani and M. van Schilfhaarde, All-electron GW approximation with the mixed basis expansion based on the full-potential LMTO method, *Solid State Commun.* **121**, 461 (2002).
- [52] T. Kotani and M. van Schilfhaarde, Fusion of the LAPW and LMTO methods: The augmented plane wave plus muffin-tin orbital method, *Phys. Rev. B* **81**, 125117 (2010).
- [53] T. Kotani, Quasiparticle self-consistent GW method based on the augmented plane-wave and muffin-tin orbital method, *J. Phys. Soc. Jpn.* **83**, 094711 (2014).
- [54] T. Kotani, H. Kino, and H. Akai, Formulation of the augmented plane-wave and muffin-tin orbital method, *J. Phys. Soc. Jpn.* **84**, 034702 (2015).
- [55] J. P. Perdew, K. Burke, and M. Ernzerhof, Generalized Gradient Approximation Made Simple, *Phys. Rev. Lett.* **77**, 3865 (1996).
- [56] A. I. Liechtenstein, V. I. Anisimov, and J. Zaanen, Density-functional theory and strong interactions: Orbital ordering in Mott-Hubbard insulators, *Phys. Rev. B* **52**, 5467(R) (1995).
- [57] S. L. Dudarev, G. A. Botton, S. Y. Savrasov, C. J. Humphreys, and A. P. Sutton, Electron-energy-loss spectra and the structural stability of nickel oxide: An LSDA+U study, *Phys. Rev. B* **57**, 1505 (1998).
- [58] K. Ooiwa, K. Endo, and A. Shinogi, A structural phase transition and magnetic properties in a Heusler alloy Ni<sub>2</sub>MnGa, *J. Magn. Magn. Mater.* **104–107**, 2011 (1992).
- [59] M. Khan, J. Brock, and I. Sugeran, Anomalous transport properties of Ni<sub>2</sub>Mn<sub>1-x</sub>Cr<sub>x</sub>Ga Heusler alloys at the martensite-austenite phase transition, *Phys. Rev. B* **93**, 054419 (2016).
- [60] U. Devarajan, S. Esakki Muthu, S. Arumugam, S. Singh, and S. R. Barman, Investigation of the influence of hydrostatic pressure on the magnetic and magnetocaloric properties of Ni<sub>2-x</sub>Mn<sub>1+x</sub>Ga (X = 0, 0.15) Heusler alloys, *J. Appl. Phys.* **114**, 053906 (2013).
- [61] A. Çakır, L. Rigbi, F. Albertini, M. Acet, M. Farle, and S. Aktürk, Extended investigation of intermartensitic transitions in Ni-Mn-Ga magnetic shape memory alloys: A detailed phase diagram determination, *J. Appl. Phys.* **114**, 183912 (2013).
- [62] P. J. Brown, A. Y. Bargawi, J. Crangle, K. U. Neumann, and K. R. Ziebeck, Direct observation of a band Jahn-Teller effect in the martensitic phase transition of Ni<sub>2</sub>MnGa, *J. Phys.: Condens. Matter* **11**, 4715 (1999).
- [63] C. P. Opeil, B. Mihaila, R. K. Schulze, L. Mañosa, A. Planes, W. L. Hults, R. A. Fisher, P. S. Riseborough, P. B. Littlewood, J. L. Smith, and J. C. Lashley, Combined Experimental and Theoretical Investigation of the Premartensitic Transition in Ni<sub>2</sub>MnGa, *Phys. Rev. Lett.* **100**, 165703 (2008).
- [64] A. Kimura, M. Ye, M. Taniguchi, E. Ikenaga, J. M. Barandiaran, and V. A. Chernenko, Lattice instability of Ni-Mn-Ga ferromagnetic shape memory alloys probed by hard X-ray photoelectron spectroscopy, *Appl. Phys. Lett.* **103**, 072403 (2013).
- [65] M. Zelený, L. Straka, M. Rameš, A. Sozinov, and O. Heczko, Origin of magnetocrystalline anisotropy in Ni-Mn-Ga-Co-Cu tetragonal martensite, *J. Magn. Magn. Mater.* **503**, 166522 (2020).
- [66] E. C. Stoner, Collective electron ferromagnetism, *Proc. R. Soc. London* **165**, 372 (1938).
- [67] Y. Takahashi, On the origin of the Curie-Weiss law of the magnetic susceptibility in itinerant electron ferromagnetism, *J. Phys. Soc. Jpn.* **55**, 3553 (1986).
- [68] E. L. Shirley, Many-body effects on bandwidths in ionic, noble gas, and molecular solids, *Phys. Rev. B* **58**, 9579 (1998).
- [69] A. Ayuela, J. Enkovaara, and R. M. Nieminen, *Ab initio* study of tetragonal variants in Ni<sub>2</sub>MnGa alloy, *J. Phys.: Condens. Matter* **14**, 5325 (2002).
- [70] B. Himmetoglu, R. M. Wentzcovitch, and M. Cococcioni, First-principles study of electronic and structural properties of CuO, *Phys. Rev. B* **84**, 115108 (2011).
- [71] A. T. Zayak, A first-principles investigation of the magnetic, structural and dynamical properties of Ni<sub>2</sub>MnGa, Ph.D. thesis, University of Duisburg-Essen, 2003.
- [72] R. Chulist and P. Czaja, On the role of atomic shuffling in the 4O, 4M and 8M martensite structures in Ni-Mn-Sn single crystal, *Scr. Mater.* **189**, 106 (2020).
- [73] A. Kundu, M. E. Gruner, M. Siewert, A. Hucht, P. Entel, and S. Ghosh, Interplay of phase sequence and electronic structure in the modulated martensites of Mn<sub>2</sub>NiGa from first-principles calculations, *Phys. Rev. B* **96**, 064107 (2017).
- [74] Y. Adachi, R. Kouta, M. Fujio, T. Kanomata, R. Y. Umetsu, X. Xu, and R. Kainuma, Magnetic phase diagram of Heusler alloy system Ni<sub>2</sub>Mn<sub>1-x</sub>Cr<sub>x</sub>Ga, *Phys. Procedia* **75**, 1187 (2015).
- [75] T. Sakon, N. Fujimoto, T. Kanomata, and Y. Adachi, Magnetostriiction of Ni<sub>2</sub>Mn<sub>1-x</sub>Cr<sub>x</sub>Ga Heusler alloys, *Metals* **7**, 410 (2017).
- [76] S. M. Shapiro, P. Vorderwisch, K. Habicht, K. Hradil, and H. Schneider, Observation of phasons in the magnetic shape memory alloy, *Europhys. Lett.* **77**, 56004 (2007).
- [77] K. Momma and F. Izumi, VESTA 3 for three-dimensional visualization of crystal, volumetric and morphology data, *J. Appl. Crystallogr.* **44**, 1272 (2011).
- [78] A. Kokalj, XCrySDen—a new program for displaying crystalline structures and electron densities, *J. Mol. Graph. Model.* **17**, 176 (1999).